Unveiling the role of counter-anions in amorphous transition metal-based oxygen evolution electrocatalysts

Xiang Wang [a,b], Xu Han [c], Ruifeng Du [a,b], Zhifu Liang [a,c], Yong Zuo [a,d], Pablo Guardia [a], Junshan Li [e], Jordi Llorca [f], Jordi Arbiol [c,g], Renji Zheng [h,i,*], Andreu Cabot [a,g,**]

[a] Catalonia Institute for Energy Research (IREC), Sant Adrià de Besòs, 08930 Barcelona, Spain
[b] Departament d'Enginyeria Electrònica i Biomèdica, Universitat de Barcelona, 08028 Barcelona, Catalonia, Spain
[c] Catalan Institute of Nanoscience and Nanotechnology (ICN2), Campus UAB, Bellaterra, 08193 Barcelona, Catalonia, Spain
[d] Istituto Italiano di Tecnologia, Via Morego 30, 16163 Genova, Italy
[e] Institute of Advanced Study, Chengdu University, Chengdu 610106, China
[f] Institute of Energy Technologies, Department of Chemical Engineering and Barcelona Research Center in Multiscale Science and Engineering, Universitat Politècnica de Catalunya, EEBE, 08019 Barcelona, Catalonia, Spain
[g] ICREA, Pg. Lluis Companys, 08010 Barcelona, Catalonia, Spain
[h] School of Minerals Processing and Bioengineering, Central South University, Changsha 410083, China
[i] Key Laboratory of Hunan Province for Clean and Efficient Utilization of Strategic Calcium-containing Mineral Resources, Central South University, Changsha 410083, China

ARTICLE INFO

ABSTRACT

At the initial stage of the oxygen evolution reaction (OER) most electrocatalysts undergo structural and chemical surface reconstruction. While this reconstruction strongly influences their performance, it is frequently overlooked. Herein, we analyze the role of the oxidized anions, which is particularly neglected in most previous works. We introduce a range of different anionic groups (Cl⁻, CH_3COO^-, NO_3^-, SO_4^{2-}) on the surface of an amorphous $ZnCo_xNi_yO_z$ catalyst by a facile proton etching and ion exchange method from a ZIF-8 self-sacrificial template. The structural and chemical properties of the obtained set of materials are thoroughly analysed and correlated with their electrocatalytic performance to study the effect of surface anionic groups, phase transition, metal leaching and defect generation on OER activity. Exploiting the control possibilities provided by the synthesis method here described and employing the uncovered property-performance correlations, the electrocatalyst is optimized. As a result, we produce $ZnCo_{1.25}Ni_{0.73}O_x$-SO_4 catalysts with outstanding OER performances, including a low overpotential of 252 mV at 10 mA cm^{-2} with a small Tafel slope of 41.6 mV dec^{-1}. Furthermore, this catalyst exhibits remarkable stability with negligible overpotential variation for 100 h. The excellent catalytic properties are rationalized using density functional theory calculations, showing that the surface-adsorbed anions, particularly SO_4^{2-}, can stabilize the OOH* intermediate, thus enhancing the OER activity. This work offers new insight into the roles of metal leaching and surface-adsorbed anions in the OER progress and facilitates the rational design of highly-efficient electrocatalysts for OER.

1. Introduction

The electrochemical oxygen evolution reaction (OER) is a vital half-reaction in several renewable energy conversion and storage technologies. OER is coupled to hydrogen evolution in electrolyzers, a metal reduction in rechargeable metal-air batteries, nitrogen reduction to ammonia, and CO_2 electroreduction to methane or methanol for instance [1–3]. However, the OER performance is dramatically hampered by the sluggish kinetics of the involved multi-electron transfer processes [4,5]. To address this critical issue, a wide range of potential OER electrocatalysts have been developed. Among them, noble metal-free transition metal oxides [6–10], nitrides [11,12], phosphides [13–15], and dichalcogenides [16,17] are particularly interesting from a cost-effectiveness point of view. However, in situ electrochemical
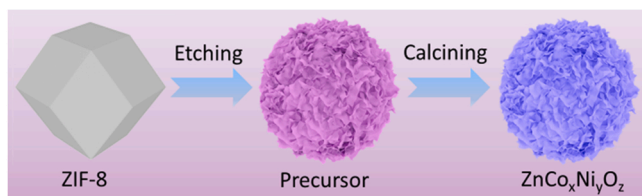
Fig. 1. Schematic illustration for the two-step preparation of ZnCo$_x$Ni$_y$O$_z$ nanosheets from ZIF-8 MOF.

analyses and *post-mortem* characterization have frequently revealed that these compounds are not the real active material in the OER process. Instead, these compounds are inevitably oxidized and reconstructed into transition metal hydroxides (M(OH)$_x$) and oxyhydroxides (MOOH) during the first steps of the electrochemical reaction [18–20]. While several pieces of evidence for this transformation have been published, the fate and role within the electrochemical cell of the anions after the pre-catalyst is oxidized is rarely reported. Besides, the extent of the transition metal transformation and the final metal reorganization and composition is hardly investigated. In particular, during the compound oxidation, it is very likely that some metal leaching occurs, which can also strongly affect the OER process.

During the reconstruction of nitrides, phosphides, sulfides and selenides, the surface anions are probably oxidized to nitrates (NO$_3^-$), phosphates (PO$_4^{3-}$), sulfates (SO$_4^{2-}$), or selenates (SeO$_4^{2-}$), respectively. In a few recent works, we and others have demonstrated such nonmetallic anionic groups play a key role in the OER activity [21–26]. Accordingly, the rational design and engineering of catalysts containing controlled amounts of such anionic groups could be an effective strategy to improve their performance. In this direction, the introduction of anionic groups *a posteriori*, through surface adsorption, generally results in a weak chemical interaction that limits the effectiveness and stability of the resultant catalyst [24]. Thus, approaches for the direct incorporation of controlled amounts of anionic groups that enable a strong bonding between anions and metal atoms need to be developed.
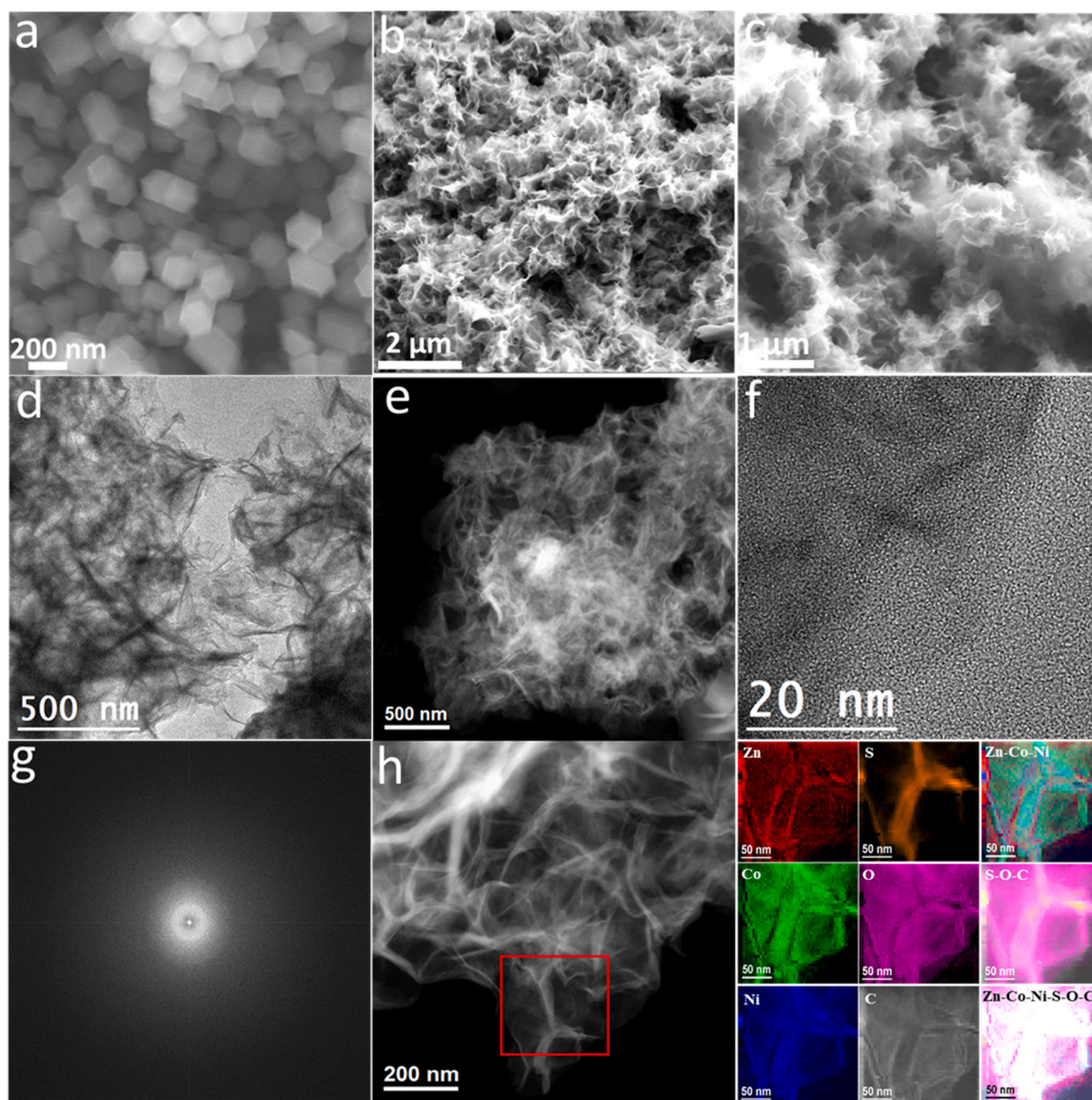

Fig. 2. (a-c) SEM images of a) ZIF-8 MOF particles, b) ZnCo$_x$Ni$_y$O$_z$-SO$_4$ precursor, and c) ZnCo$_x$Ni$_y$O$_z$-SO$_4$ nanosheets. d) TEM image, e) HAADF STEM image, f) HRTEM image, g) corresponding power spectrum (FFT) and h) HAADF STEM images and EELS chemical composition maps of ZnCo$_x$Ni$_y$O$_z$-SO$_4$ nanosheets. The EELS maps were obtained from the red squared area on the left HAADF STEM micrograph (left). Individual Zn L$_{2,3}$-edges at 1020 eV (red), Co L$_{2,3}$-edges at 779 eV (green), Ni L$_{2,3}$-edges at 855 eV (blue), S L$_{2,3}$-edges at 165 eV (orange), O K-edges at 532 eV (pink) and C K-edges at 285 eV (gray) and composites of Zn-Co-Ni, S-O-C and Zn-Co-Ni-S-O-C.
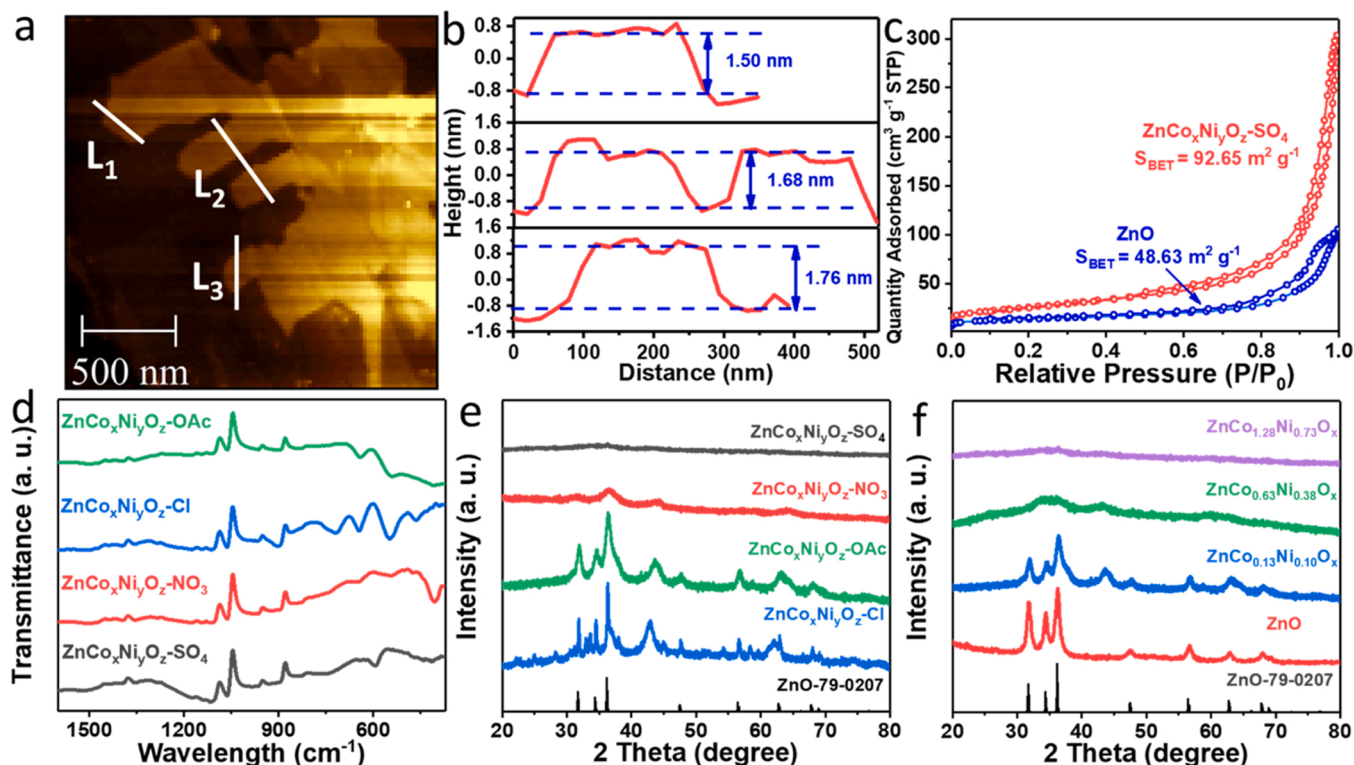
Fig. 3. a) AFM images and b) the corresponding thickness measurement data of $ZnCo_{1.26}Ni_{0.73}O_x$-SO_4 Nanosheets. c) N_2 adsorption-desorption isotherms for $ZnCo_{1.26}Ni_{0.73}O_x$-SO_4 and ZnO. d) FTIR spectra and e) XRD patterns of $ZnCo_xNi_yO_z$ obtained from different anions. f) XRD pattern of $ZnCo_xNi_yO_z$-SO_4 with different metal content.

At the same time, amorphous catalysts generally display improved OER performance over their crystalline counterpart [27,28]. Amorphous catalysts offer higher flexibility in terms of composition and atomic arrangement, which allows for more facile incorporation of a wide range and concentration of extrinsic dopants [29]. A higher variety of oxidation states of multivalence metals is also possible in amorphous structures, which contain more unsaturated coordination spheres [30]. Besides, amorphous oxides are also generally characterized by less strongly bond oxygen ions compared with crystalline materials, which can facilitate an efficient lattice oxygen-mediated OER mechanism [31, 32].

Beyond the abundant structural defects found in amorphous materials, the leaching of controlled amounts of the composing transition metal ions can be also beneficial. Controlled leaching can in situ generate additional defects that may translate into active OER sites [22, 33–36].

Herein, we introduce different anionic groups (Cl^{-}, CH$_3$COO[-], NO$_3^-$, SO$_4^{2-}$) in $ZnCo_xNi_yO_z$ nanosheets by a facile proton etching and ion exchange method. We test the resulting materials for OER and study the material transformation during the reaction, including metal ion leaching. We thoroughly analyze the structural and chemical properties of the initial and evolved materials and correlate them with their electrocatalytic performance. Exploiting the control possibilities provided by the synthesis method and taking advantage of the uncovered property-performance correlations, the electrocatalyst is optimized. Additionally, the high performance of the optimized catalyst is analysed using density functional theory (DFT) calculations, which allows for determining the influence of particular surface-adsorbed groups on the OER activity.

2. Material and methods

2.1. Chemicals

Zinc nitrate hexahydrate ($Zn(NO_3)_2 \cdot 6H_2O$), cobalt nitrate hexahydrate ($Co(NO_3)_2 \cdot 6H_2O$, 99.9%), nickel nitrate hexahydrate ($Ni(NO_3)_2 \cdot 6H_2O$), cobalt chloride hexahydrate ($CoCl_2 \cdot 6H_2O$, 98%), nickel chloride hexahydrate ($NiCl_2 \cdot 6H_2O$, 98%), cobalt acetate tetrahydrate ($Co(CH_3COO)_2$, 98%), nickel(II) acetate tetrahydrate ($Ni(CH_3COO)_2$, 98%), cobalt sulfate hexahydrate ($CoSO_4 \cdot 6H_2O$, 99%), nickel sulfate hexahydrate ($NiSO_4 \cdot 6H_2O$, 99%), potassium hydroxide (KOH, 85%), and 2-methylimidazole ($C_4H_6N_2$, 99%) were purchased from Acros Organics. Ruthenium(IV) oxide (RuO_2, 99.9% metal basis) and Nafion (5 wt% in a mixture of low aliphatic alcohols and water) were obtained from Sigma-Aldrich. Methanol, ethanol and isopropanol were of analytical grade and obtained from various sources. Milli-Q water was obtained from a Purelab flex from Elga. All chemicals were used as received, without further purification.

2.2. Zeolitic imidazolate framework (ZIF-8) MOF

MOFs are crystalline materials with an ordered topological structure that are often used as a template for the engineering of porous nanostructured electrocatalysts [37,38]. Among the different MOFs, we selected the ZIF-8 due to its high versatility and ease of synthesis. The synthesis of ZIF-8 was based on a previous procedure with modifications [39]. Typically, 0.87 g $Zn(NO_3)_2 \cdot 6 H_2O$ was dissolved in 30 mL methanol to obtain a clear solution. Subsequently, the above solution was poured into 30 mL methanol containing 1.97 g 2-methylimidazole under vigorous stirring. After mixing completely, the solution was incubated for 24 h at room temperature. White precipitates were collected by centrifugation, washed with methanol at least three times, and dried at 60 °C overnight.
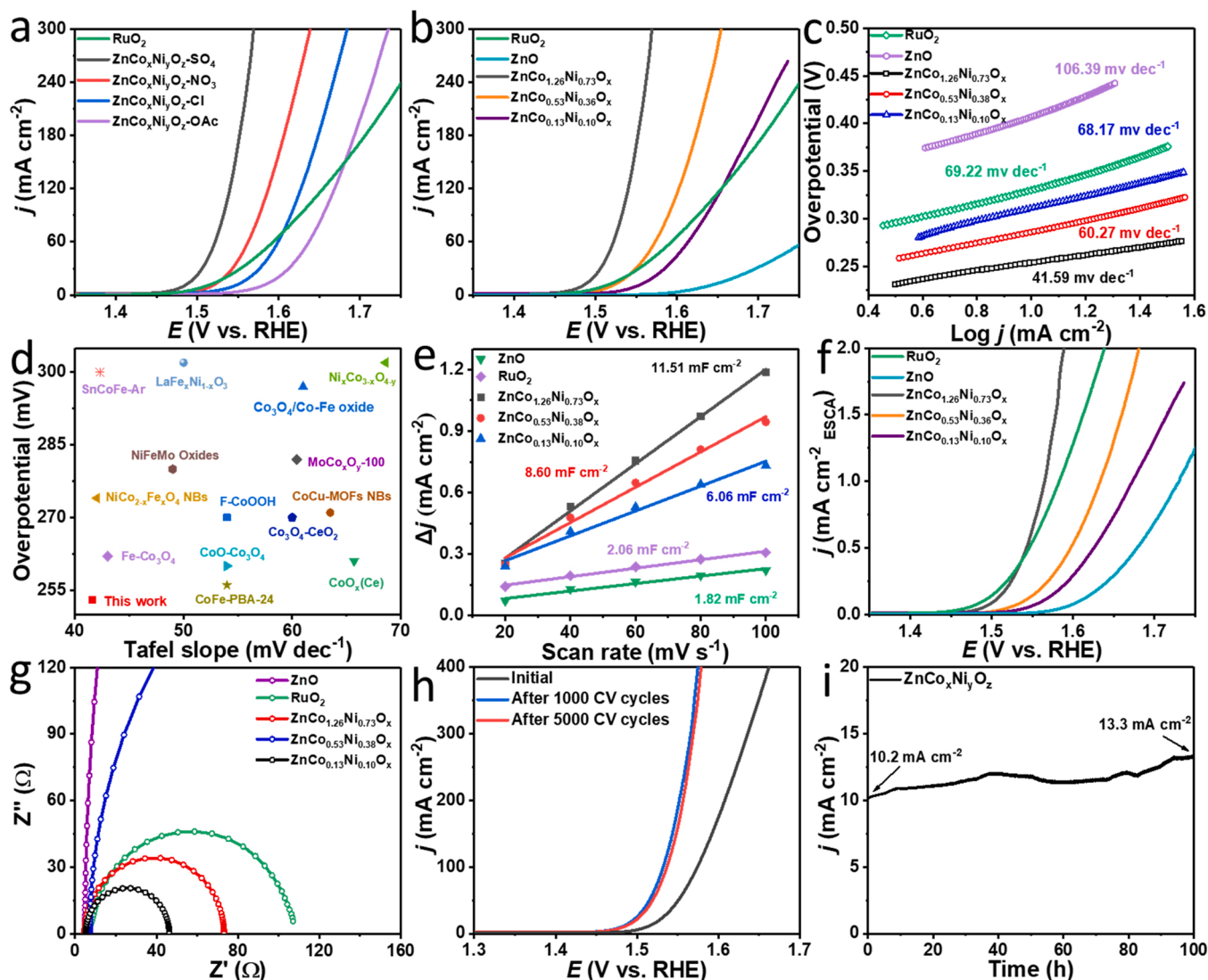
Fig. 4. Electrocatalytic OER performance of the various catalysts. a-b) LSV curves of $ZnCo_xNi_yO_z$-M and $ZnCo_xNi_yO_z$-SO_4. c) Tafel plots. d) Comparison of overpotential at 10 mA cm^{-2} and Tafel slopes for $ZnCo_{1.26}Ni_{0.73}O_x$–SO_4 and some cobalt-based OER catalysts (Table S3). e) Capacitive current density measured at 1.17 V vs. RHE plotted as a function of scan rate. f) ECSA-normalized OER polarization curves. g) Nyquist plots at the potential of 1.52 V vs. RHE. h) LSV curves of $ZnCo_{1.26}Ni_{0.73}O_x$–SO_4 after 1000 and 5000 cycles. i) chronoamperometry curve of $ZnCo_{1.26}Ni_{0.73}O_x$–SO_4.

2.3. Synthesis of ZnCoxNiyOz

100 mg of as-prepared ZIF-8 powder was ultrasonically re-dispersed in 20 mL of ethanol. Then, this solution was poured into a 100 mL aqueous solution containing 300 mg $CoSO_4 0.6 H_2O$ and 300 mg $NiSO_4 0.6 H_2O$ under continuous magnetic stirring. The mixture was stirred vigorously for 12 h at room temperature. Precipitates were collected by centrifugation, washed with water at least three times, and freeze-dried overnight. The obtained products were calcined in the muffle furnace at 350 °C for 2 h under an air atmosphere. The final products were obtained after natural cooling to room temperature and denoted as $ZnCo_xNi_yO_z$-SO_4. Besides, $ZnCo_xNi_yO_z$-NO_3, $ZnCo_xNi_yO_z$-OAc, and $ZnCo_xNi_yO_z$-Cl were obtained using the same method, but substituting sulfates with equal amounts of chlorides, acetates, and nitrates, respectively. As a reference material, ZnO nanoparticles were obtained by the direct calcination of ZIF-8. Besides, $ZnCo_xNi_yO_z$-SO_4 samples with different metal contents were obtained by adjusting the amount of cobalt and nickel salts added. Table S5 lists all the produced samples.

3. Results and discussion

3.1. Synthesis and characterizations of catalysts

Fig. 1 illustrates the two-step approach used to produce $ZnCo_xNi_yO_z$ from a self-sacrificial ZIF-8 template (see details in the experimental section). In the first step, the Zn-based ZIF-8 MOF is reacted with Ni and Co salts (sulfates, nitrates, chlorides or acetates). In this process, the protons produced by the metal cation (Co^{2+}, Ni^{2+}) hydrolysis ($M^{2+} + 2 H_2O = M(OH)_2 + 2 H^+$) etch the ZIF-8, dissociating its polyhedron structure [40,41]. At the same time, the cobalt and nickel ions partially replace zinc within the structure. Meanwhile, the salt anions (SO_4^{2-}, NO_3^-, Cl^-, OAC^-) are anchored to the material surface by exchange with the MOF organic ligands. Fig. 2a displays a representative SEM image of the ZIF-8 template, which is characterized by a smooth rhombic dodecahedron morphology with a uniform particle size of about 100 nm. Upon reaction with the transition metal sulfate, a nanosheet-like structure progressively expands around the gradually disappearing ZIF-8 template (Fig. 2b). Eventually, the dodecahedron template has fully disappeared and only the porous nanosheet structure is observed. Fig. S1 shows a scheme of the etching evolution with time and SEM images of the
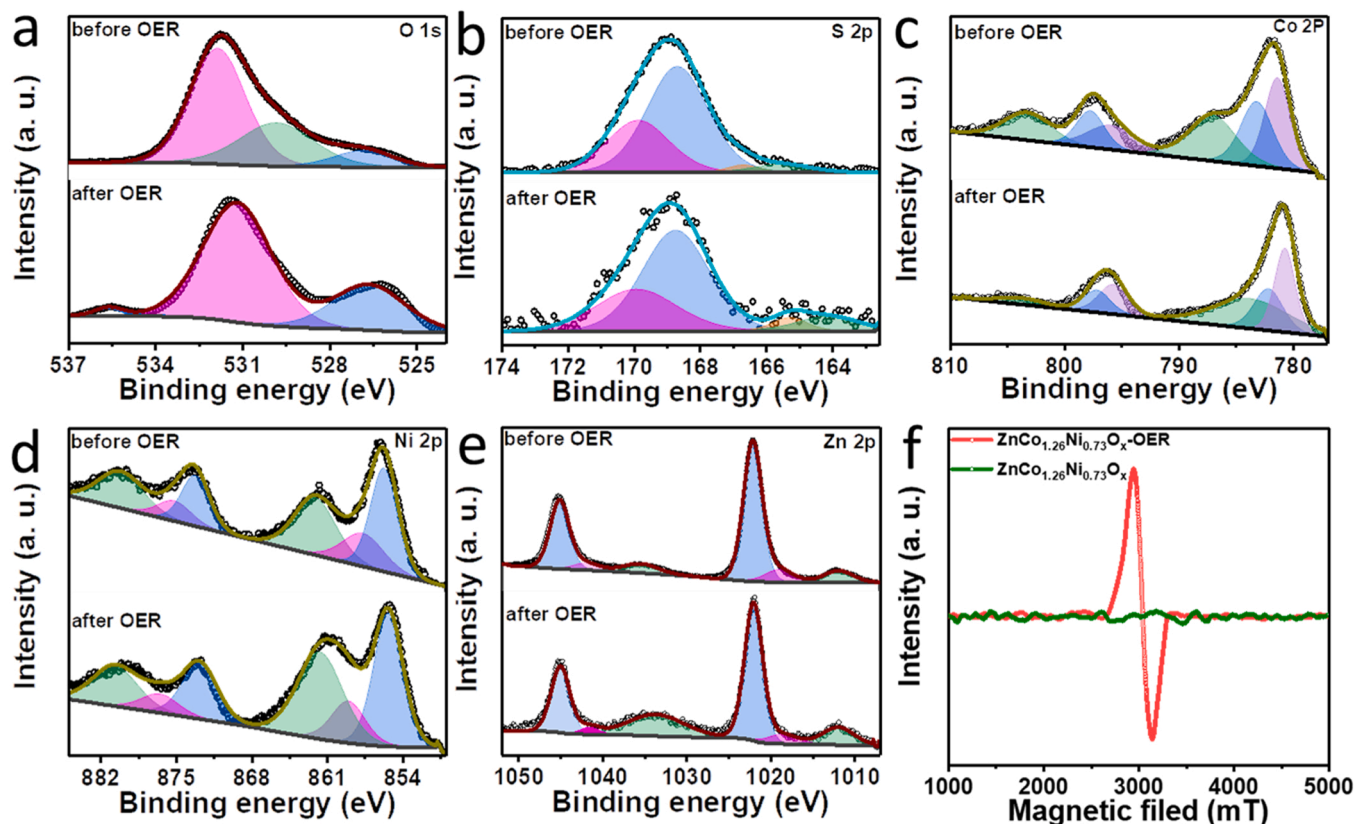
Fig. 5. a-e) O 1s, S 2p, Co 2p, Ni 2p and Zn 2p high resolution XPS spectra. f) EPR spectrum of $ZnCo_{1.26}Ni_{0.73}O_x$-SO_4 before and after OER.

product obtained after 1, 3, and 12 h etching.

In the second step, the material is annealed under air to form an amorphous oxide. Figs. 2c-e and S2 show SEM, TEM and STEM images of the ultrathin nanosheets with wrinkled structures obtained after annealing the material at 350 °C in an air atmosphere. HRTEM images and the corresponding indexed fast Fourier transform (FFT) crystallographic analyses confirmed that the annealed $ZnCo_xNi_yO_z$-SO_4 nanosheets presented an amorphous structure with no crystallographic ordering (Fig. 2f,g). Meanwhile, HAADF-STEM and EELS compositional maps showed C, N, O, S, Zn, Co and Ni to be homogeneously distributed throughout the nanosheets (Figs. 2h and S3). Besides, ICP-MS and EDX allowed determining the metal ratios (Table S1).

Fig. 3a shows an AFM image of the $ZnCo_xNi_yO_z$-SO_4 nanosheets. From the height line profiles of some of the nanosheets shown in Fig. 3a, their average thickness was estimated at 1.7 ± 0.2 nm (Fig. 3b). From the N_2 adsorption-desorption isotherms displayed in Fig. 3c, the Brunauer-Emmett-Teller (BET) surface area of $ZnCo_xNi_yO_z$-SO_4 was estimated at 93 $m^2\,g^{-1}$, almost twice that of ZnO particles obtained from the annealing of ZIF-8 (49 $m^2\,g^{-1}$). Besides, the Barrett-Joyner-Halenda (BJH) average pore size and cumulative pore volume were 19.1 nm and 0.47 $cm^3\,g^{-1}$ for $ZnCo_xNi_yO_z$-SO_4, and 18.1 nm and 0.16 $cm^3\,g^{-1}$ for ZnO particles (Fig. S4). Such nanosheet morphology and mesoporous structure dramatically increase the percentage of surface unsaturated atoms, providing a high potential electroactive surface area, while at the same time facilitating the rapid diffusion of reactants and reaction products.

Fig. 3d displays the FTIR spectra of $ZnCo_xNi_yO_z$ samples with different anions. $ZnCo_xNi_yO_z$-SO_4 displayed an evident FTIR absorption peak at about 600 cm^{-1}, which is a fingerprint of the presence of SO_4^{2-} ions [42] The peaks at about 400, 550, and 640 cm^{-1} can be assigned to nitrate, chloride, and acetate, respectively (Fig. S5 and Table S2) [43]. The anionic groups played an important role in determining the crystallinity, morphology and composition of the obtained material, as

evidenced by XRD, SEM and EDX analysis of $ZnCo_xNi_yO_z$ obtained with the different precursors (Figs. 3e and S6–S9). Protons react with the surface of ZIF-8, breaking the coordinative bond between Zn^{2+} and 2-methylimidazole linkers in the ZIF-8, thus etching the MOF and releasing Zn^{2+} ions into the solution [39]. Thus, we hypothesize that the crystallinity and architecture dependence on the used anion may be related to the different pH resulting from the hydrolysis of the different anions. To confirm this hypothesis, the pH of the solutions obtained from the dissolution of the same amount of different anionic metal salts was determined. The smallest pH value was obtained with the SO_4^{2-} (4.36) and increased in the following order: NO_3^-(5.75), Cl^-(7.02), and OAC^-(7.82). Such different pH values strongly determine the extent of MOF etching, thus affecting the crystallinity, morphology and also composition of the products. We observed that the lower the pH value, the weaker the crystallinity, the more favorable formation of nanosheets, and the lower Zn content on the final material.

In the same direction, the salt concentration also played an important role. Figs. 3f, S6, S11 and S12 show the XRD patterns, SEM images and EDX spectra of $ZnCo_xNi_yO_z$-SO_4 obtained using different concentrations of Ni and Co sulfates. When increasing the metal salt concentration, deeper hydrolysis and etching take place, which translates into a more amorphous structure, a more favorable nanosheet growth and a lower Zn content.

3.2. OER performance

The OER activity of $ZnCo_xNi_yO_z$ modified with different anions was initially assessed using LSV with a conventional three-electrode set-up in a 1 M KOH electrolyte. A commercial RuO_2 electrocatalyst was also tested as a reference. As shown in Fig. 4a, the iR-compensated LSV curve of $ZnCo_xNi_yO_z$-SO_4 showed a very small overpotential at 10 mA cm^{-2} (η^{10}), just 252 mV, well below that of $ZnCo_xNi_yO_z$-NO_3 (287 mV), $ZnCo_xNi_yO_z$-Cl (314 mV), $ZnCo_xNi_yO_z$-OAc (348 mV) and RuO_2
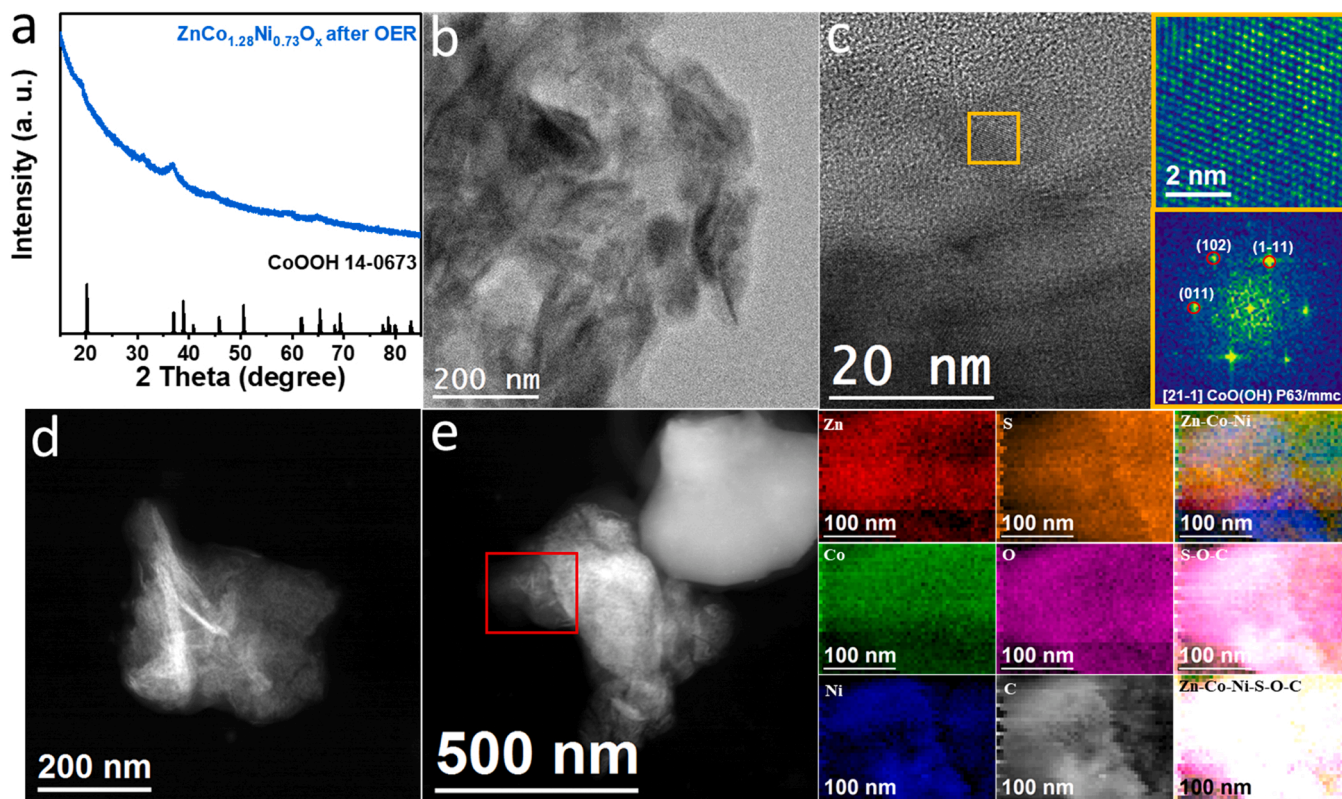
Fig. 6. a) XRD pattern, b) TEM images, c) HRTEM and corresponding power spectrum (FFT), d) HAADF STEM image and e) HADDF EELS image together with the corresponding EELS chemical composition maps of $ZnCo_{1.26}Ni_{0.73}O_x–SO_4$ after OER. The EELS maps were obtained from the red squared area on the left HAADF STEM micrograph. Individual Zn $L_{2,3}$-edges at 1020 eV (red), Co $L_{2,3}$-edges at 779 eV (green), Ni $L_{2,3}$-edges at 855 eV (blue), S $L_{2,3}$-edges at 165 eV (orange), O K-edges at 532 eV (pink) and C K-edges at 284 eV (gray) and composites of Zn-Co-Ni, S-O-C and Zn-Co-Ni-S-O-C.

(280 mV). The significant differences in overpotential demonstrate the important role played by the metal precursor counterions. Besides, by modifying the cobalt and nickel content, we determined the best OER performance to be obtained with a $ZnCo_{1.26}Ni_{0.73}O_x$-SO$_4$ composition (Fig. 4b). In contrast, the ZnO produced from the annealing of the ZIF-8 was characterized by a much poorer performance with a η^{10} of 407 mV at 10 mA cm^{-2}.

Fig. 4c displays the Tafel plots of the different catalysts. The $ZnCo_{1.26}Ni_{0.73}O_x$-SO$_4$ exhibited the smallest Tafel slope (41.6 mV dec^{-1}) among all the tested catalysts, including commercial RuO$_2$, thus demonstrating the fastest reaction kinetics. $ZnCo_{1.26}$-$Ni_{0.73}O_x$-SO$_4$ also exhibited outstanding OER activity and kinetics when compared to some previously reported oxide-based OER electrocatalysts (Fig. 4d and TableS3).

The ECSA was estimated from the double-layer capacitance (C$_{dl}$) measured by CV at different scanning rates (Fig. S13a-e). C$_{dl}$ was calculated from the slope of the linear fitting of the charge current versus the scan rate (Fig. 4e, Table S4) [30,44]. Using a specific capacity of 0.04 mF cm^{-2}, ECSA was estimated at 288 cm^2 for $ZnCo_{1.26}Ni_{0.73}O_x$-SO$_4$, well above that of the other catalysts evaluated (Table S4) [45]. Fig. 4f displays the specific activity obtained by normalizing the current to the ECSA. Despite its much larger ECSA, $ZnCo_{1.26}Ni_{0.73}O_x$-SO$_4$ also displayed the highest specific activity. We hypothesize this excellent activity to be related to a combination of different parameters, including a proper Zn/Co/Ni ratio, the presence of sulfate ions at the catalyst surface, its amorphous structure and its highly porous nanosheet-based architecture.

The charge transfer rate at the catalyst reaction interface was evaluated by EIS [46]. Nyquist plots show the charge transfer resistance (R$_{ct}$) of $ZnCo_{1.26}Ni_{0.73}O_x$-SO$_4$ to be the smallest among all the tested samples (Fig. 4g), which point to a faster charge transfer rate in this material, in

good agreement with the smallest Tafel slope.

Fig. 4h shows the initial LSV curve and the LSV profiles of $ZnCo_x$-Ni_yO_z-SO$_4$ after 1000 and 5000 CV cycles. The overpotential needed to catalyze water oxidation at 10 mA cm^{-2} after 1000 and 5000 cycles test was virtually the same. This overpotential was much lower than that displayed on the first LSV curve. The chronoamperometry (i-t) durability test for $ZnCo_xNi_yO_z$-SO$_4$ at the initial overpotential showed a relatively stable and even increasing current density during 100 h of continuous operation (Fig. 4i), indicating that the $ZnCo_{1.26}Ni_{0.73}O_z$-SO$_4$ electrocatalysts have excellent stability under the electrochemical conditions of water oxidation.

We hypothesize the overpotential decrease during the first cycles and the gradual increase of current density measured in the chronoamperometry test to be associated with progressive leaching of zinc ions. To test this hypothesis, the dissolution rate of different elements was monitored by analyzing the metal content within the electrolyte using ICP-MS. As shown in Fig. S13f, negligible amounts of Co and Ni were dissolved during the 18 h chronoamperometric test. In contrast, a significant increase in the Zn concentration was detected within the electrolyte during the first 12 h of the reaction. The leaching of Zn initially generates metal vacancies and active sites within the reconstituted electrocatalyst, which can promote the OER performance [36].

3.3. Structural and chemical evolution

To further reveal the parameters behind the excellent OER catalytic activity, the surface composition and chemical states of $ZnCo_{1.26}$-$Ni_{0.73}O_z$-SO$_4$ before and after the OER test were characterized by XPS (Fig. 5). The high-resolution O 1 s XPS spectra of $ZnCo_{1.26}Ni_{0.73}O_z$-SO$_4$ showed the OER test to result in a negative shift of the lattice oxygen (O$_L$) signal located at 529.7 eV (Fig. 5a). We associate this shift to the
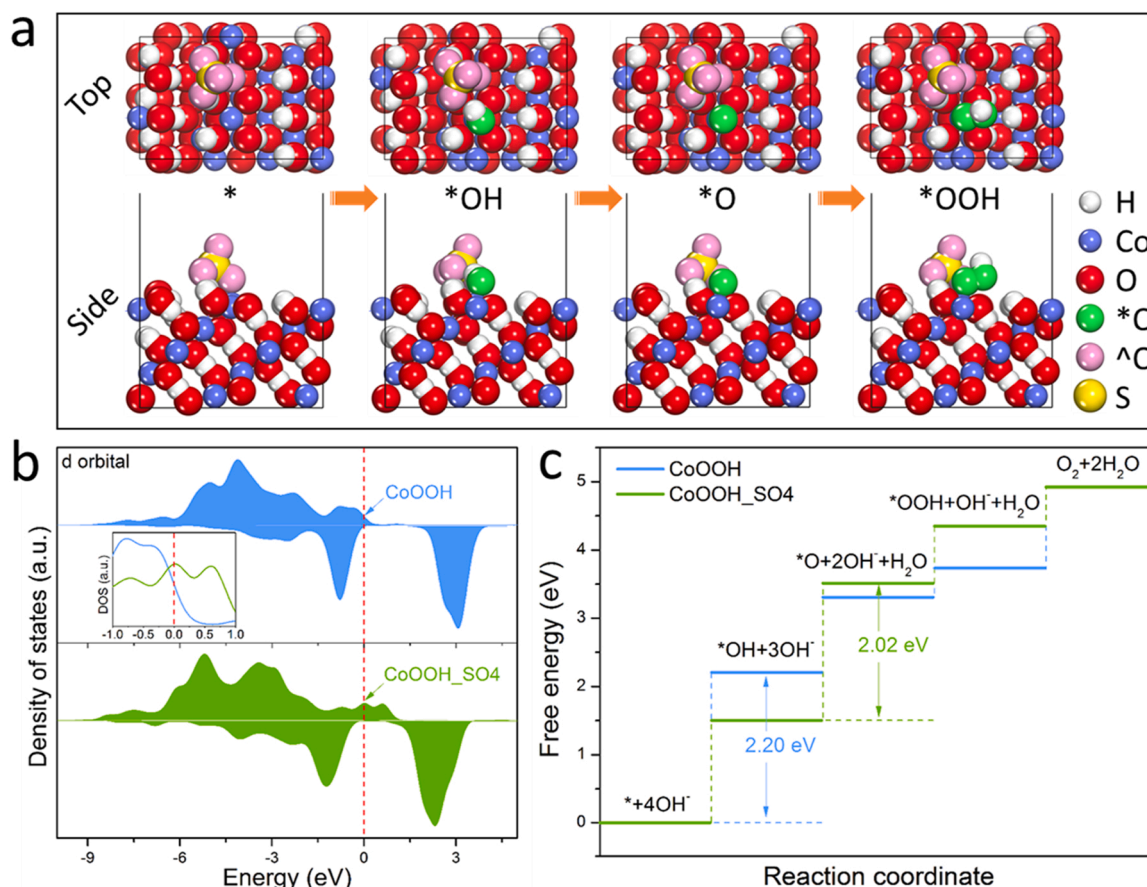
Fig. 7. a) Optimized structural models of CoOOH-SO$_4$ for different OER steps. White balls represent hydrogen atoms, blue balls are cobalt atoms, yellow balls stand for sulfur atoms, red balls represent the oxygen in the catalyst structure, green balls are the oxygen adsorbed on the intermediate, and pink balls are oxygen on the sulfate group. b) DOS of CoOOH and CoOOH-SO$_4$ regarding the Co 3d orbitals. c) Gibbs free energy diagrams of OER intermediates over CoOOH and CoOOH-SO$_4$.

formation of surface metal (oxy)hydroxide that increases the electron density around the lattice O [47–49]. In addition, the O 1 s peak at 531.5 eV, associated with surface hydroxide (OH$_L$), negatively shifted by 0.35 eV after the OER test. The OH$_L$/O$_L$ ratio in the post-OER catalyst (2.50) was significantly higher than that in the pristine ZnCo$_{1.26}$-Ni$_{0.73}$O$_z$-SO$_4$ (2.03) [19]. Interestingly, a clear S 2p XPS signal associated with sulfur within a sulfate chemical environment (S 2p$_{3/2}$ = 168.7 eV) was measured both before and after the OER test (Fig. 5b). Besides satellite peaks, two Co components were observed in the Co 2p spectra, and both shifted to lower binding energies after the OER, from 780.7 eV to 780.5 eV for Co^{2+} (Co 2p$_{3/2}$) and from 782.4 eV to 782.1 eV for the Co^{3+} (Co 2p$_{3/2}$) component (Fig. 5c). Additionally, the ratio Co^{3+}/Co^{2+} increased during OER, from 1.1 to 1.5, indicating the formation of additional CoOOH species on the surface [34]. In the Ni 2p spectrum (Fig. 5d), the Ni 2p$_{3/2}$ peak was deconvoluted into two main peaks at 855.7 and 857.6 eV, corresponding to Ni^{2+} and Ni^{3+} [42]. After OER, the Ni 2p$_{3/2}$ peaks had shifted about 0.6 eV. Besides, the relative percentage of Ni^{3+} on the surface greatly increased from 36% to 49%, denoting the transition of nickel species from oxides to (oxy)hydroxide [50]. Notably, the XPS signals of Zn became weaker with the OER, as observed from the higher noise in the Zn 2p spectrum after OER (Fig. 5e), which is consistent with Zn leaching in the alkaline medium observed by ICP-MS [50] This Zn leaching can favor the conversion of cobalt and Ni oxide on the surface of ZnCo$_x$Ni$_y$O$_z$ to CoO$_x$(OH)$_y$ and NiO$_x$(OH)$_y$ species [51,52]. Overall, XPS results confirmed the surface reconstruction of ZnCo$_{1.26}$Ni$_{0.73}$O$_z$-SO$_4$ during OER, chemically evolving from a surface metal oxide to metal (oxy)hydroxide species and loosing Zn during the process [53].

The EPR spectra of ZnCo$_{1.23}$Ni$_{0.73}$O$_x$-SO$_4$ before and after OER were measured to explore species with unpaired electrons (Fig. 5f) [54,55]. We observed the signal at g = 2.12, associated with the presence of oxygen vacancies V$_O$, to be strongly enhanced after OER test. Thus, a large density of oxygen vacancies was generated during OER, which is potentially associated with zinc leaching, and which can favor the OER catalytic activity by introducing higher energy dangling bonds at the catalyst surface [56,57].

After OER, XRD and HRTEM analysis of ZnCo$_{1.26}$Ni$_{0.73}$O$_z$-SO$_4$ displayed the presence of the CoOOH crystal phase, formed during OER (Fig. 6a-c). SEM and TEM images exhibited the ultrathin nanosheet morphology to be maintained during the OER test (Figs. S14 and S15). HAADF-STEM images and EELS elemental maps (Fig. 6d-e) demonstrated a homogeneous distribution of O, S, Zn, Co, and Ni within the cycled material. Besides, the comparison of the ZnCo$_{1.26}$Ni$_{0.73}$O$_z$-SO$_4$ composition before and after OER, as determined by EDX, ICP-MS and XPS analyses, showed a strong decrease in the amount of zinc (Table S1).

3.4. DFT calculations

DFT calculations were performed to better understand the role of surface SO$_4^{2-}$ on the enhancement of the OER activity. Owing to the complexity of the ZnCo$_{1.23}$Ni$_{0.73}$O$_x$-SO$_4^{2-}$ amorphous structure, we used a cobalt oxohydroxide surface as a model system. To build the rational structural models for OER, the dominant active sites of CoOOH and CoOOH-SO$_4$ during OER were first determined, and the density of state (DOS) and different charge density were investigated. Figs. 7a and S16a, S17 show the optimized structural models of CoOOH-SO$_4$ and CoOOH for different OER steps. As displayed in Fig. 7b, with the adsorption of the SO$_4^{2-}$, the contribution of the Co 3d orbital to the DOS at the Fermi

level strongly increases [23,58].

The Gibbs free energies of OER pathways on CoOOH-SO$_4$ and CoOOH are displayed in Figs. 6b and S16b,c. The formation of OOH* was determined to be the rate-determining step (RDS) on CoOOH. In the presence of the sulfate ion, CoOOH-SO$_4$ displayed a much lower free energy for OOH* generation when compared with CoOOH, which is consistent with the higher OER activity experimentally measured for this material [21,59].

4. Conclusions

In summary, the influence of several counterions on the structural, chemical and functional properties of ZnCo$_{1.23}$Ni$_{0.73}$O$_x$ electrocatalyst was analyzed. Materials were produced via a facile etching and annealing methods using ZIF-8 as a self-sacrificial template. ZnCo$_{1.23}$-Ni$_{0.73}$O$_x$-SO$_4$ displayed remarkable OER performances with a low Tafel slope of 41.6 mV dec^{-1}, ultralow overpotential of 252 mV for 10 mA cm^{-2}, and high stability during 100 h continuous operation. The high OER activity is associated with several factors, including the presence of oxygen vacancies, zinc leaching and the presence of sulfate anions. CV, I-T, XPS and EPR results indicate the simultaneous leaching of Zn, formation of oxygen vacancies and electrochemical surface reconstruction to CoOOH active species. DFT calculations proved that the decorated SO$_4^{2-}$ facilitates the formation of OOH* on CoOOH active sites, thus accelerating the OER process. This work offers new insights into the fate and effect of counter anions on OER performance and paves a new avenue for developing highly efficient electrocatalysts.

CRediT authorship contribution statement

Xiang Wang: Conceptualization, Methodology, Validation, Investigation, Formal analysis, Data curation, Visualization, Writing – original draft, Writing – review & editing. **Ruifeng Du** and **Zhifu Liang**: Methodology, Formal analysis, Data curation. **Yong Zuo**: Investigation, ICP-MS testing and analysis. **Pablo Guardia**: SEM and TEM characterization, Supervision. **Xu Han** and **Jordi Arbiol**: HRTEM, HAADF-STEM EELS characterization and analysis, Supervision. **Junshan Li:** Formal analysis, Visualization. **Jordi Llorca**: XPS characterization and analysis, Supervision. **Renji Zheng**: Computations, DFT simulation and construction calculations, Supervision. **Andreu Cabot**: Supervision, Writing – review & editing, Project administration, Funding acquisition.

Declaration of Competing Interest

The authors declare that they have no known competing financial interests or personal relationships that could have appeared to influence the work reported in this paper.

Data availability

Data will be made available on request.

Acknowledgments

Appendix A. Supplementary material

Supplementary data associated with this article can be found in the online version at doi:10.1016/j.apcatb.2022.121988.

References

[1] J. Song, C. Wei, Z.F. Huang, C. Liu, L. Zeng, X. Wang, Z.J. Xu, A review on fundamentals for designing oxygen evolution electrocatalysts, Chem. Soc. Rev. 49 (2020) 2196–2214.

[2] J. Du, F. Li, L. Sun, Metal-organic frameworks and their derivatives as electrocatalysts for the oxygen evolution reaction, Chem. Soc. Rev. 50 (2021) 2663–2695.

[3] K. Wang, X. Wang, Z. Li, B. Yang, M. Ling, X. Gao, J. Lu, Q. Shi, L. Lei, G. Wu, Y. Hou, Designing 3d dual transition metal electrocatalysts for oxygen evolution reaction in alkaline electrolyte: beyond oxides, Nano Energy 77 (2020), 105162.

[4] L. Gao, X. Cui, C.D. Sewell, J. Li, Z. Lin, Recent advances in activating surface reconstruction for the high-efficiency oxygen evolution reaction, Chem. Soc. Rev. 50 (2021) 8428–8469.

[5] Z.P. Wu, X.F. Lu, S.Q. Zang, X.W. Lou, Non-noble-metal-based electrocatalysts toward the oxygen evolution reaction, Adv. Funct. Mater. 30 (2020), 1910274.

[6] M. Yu, E. Budiyanto, H. Tuysuz, Principles of water electrolysis and recent progress in cobalt-, nickel-, and iron-based oxides for the oxygen evolution reaction, Angew. Chem. Int. Ed. 61 (2022), e202103824.

[7] H. Wang, K.H. Zhang, J.P. Hofmann, A. Victor, F.E. Oropeza, The electronic structure of transition metal oxides for oxygen evolution reaction, J. Mater. Chem. A 9 (2021) 19465–19488.

[8] X. Xu, Y. Pan, Y. Zhong, C. Shi, D. Guan, L. Ge, Z. Hu, Y.Y. Chin, H.J. Lin, C.T. Chen, H. Wang, S.P. Jiang, Z. Shao, New undisputed evidence and strategy for enhanced lattice-oxygen participation of perovskite electrocatalyst through cation deficiency manipulation, Adv. Sci. 9 (2022), e2200530.

[9] H. Sun, X. Xu, H. Kim, W. Jung, W. Zhou, Z. Shao, Electrochemical water splitting: bridging the gaps between fundamental research and industrial applications, Energy Environ. Mater. (2022), e12441.

[10] D. Guan, J. Zhong, H. Xu, Y.-C. Huang, Z. Hu, B. Chen, Y. Zhang, M. Ni, X. Xu, W. Zhou, Z. Shao, A universal chemical-induced tensile strain tuning strategy to boost oxygen-evolving electrocatalysis on perovskite oxides, Appl. Phys. Rev. 9 (2022), 011422.

[11] H. Wang, J. Li, K. Li, Y. Lin, J. Chen, L. Gao, V. Nicolosi, X. Xiao, J.M. Lee, Transition metal nitrides for electrochemical energy applications, Chem. Soc. Rev. 50 (2021) 1354–1390.

[12] A.K. Tareen, G.S. Priyanga, K. Khan, E. Pervaiz, T. Thomas, M. Yang, Nickel-based transition metal nitride electrocatalysts for the oxygen evolution reaction, ChemSusChem 12 (2019) 3941–3954.

[13] J. Xu, J. Li, D. Xiong, B. Zhang, Y. Liu, K.H. Wu, I. Amorim, W. Li, L. Liu, Trends in activity for the oxygen evolution reaction on transition metal (M = Fe, Co, Ni) phosphide pre-catalysts, Chem. Sci. 9 (2018) 3470–3476.

[14] A. Parra-Puerto, K.L. Ng, K. Fahy, A.E. Goode, M.P. Ryan, A. Kucernak, Supported transition metal phosphides: activity survey for HER, ORR, OER, and corrosion resistance in acid and alkaline electrolytes, ACS Catal. 9 (2019) 11515–11529.

[15] C. Wang, W. Chen, D. Yuan, S. Qian, D. Cai, J. Jiang, S. Zhang, Tailoring the nanostructure and electronic configuration of metal phosphides for efficient electrocatalytic oxygen evolution reactions, Nano Energy 69 (2020), 104453.

[16] X. Wu, H. Zhang, J. Zhang, X.W.D. Lou, Recent advances on transition metal dichalcogenides for electrochemical energy conversion, Adv. Mater. 33 (2021), 2008376.

[17] J. Yin, J. Jin, H. Lin, Z. Yin, J. Li, M. Lu, L. Guo, P. Xi, Y. Tang, C.H. Yan, Optimized metal chalcogenides for boosting water splitting, Adv. Sci. 7 (2020), 1903070.

[18] S. Jin, Are metal chalcogenides, nitrides, and phosphides oxygen evolution catalysts or bifunctional catalysts? ACS Energy Lett. 2 (2017) 1937–1938.

[19] Y. Liu, X. Luo, C. Zhou, S. Du, D. Zhen, B. Chen, J. Li, Q. Wu, Y. Iru, D. Chen, A modulated electronic state strategy designed to integrate active HER and OER components as hybrid heterostructures for efficient overall water splitting, Appl. Catal. B 260 (2020), 118197.

[20] X. Gu, Z. Liu, M. Li, J. Tian, L. Feng, Surface structure regulation and evaluation of FeNi-based nanoparticles for oxygen evolution reaction, Appl. Catal. B 297 (2021), 120462.

[21] H. Liao, T. Luo, P. Tan, K. Chen, L. Lu, Y. Liu, M. Liu, J. Pan, Unveiling role of sulfate ion in nickel-iron (oxy)hydroxide with enhanced oxygen-evolving performance, Adv. Funct. Mater. 31 (2021), 2102772.

[22] H. Meng, W. Xi, Z. Ren, S. Du, J. Wu, L. Zhao, B. Liu, H. Fu, Solar-boosted electrocatalytic oxygen evolution via catalytic site remodelling of CoCr layered double hydroxide, Appl. Catal. B 284 (2021), 119707.

[23] R. Zhang, L. Wang, L. Pan, Z. Chen, W. Jia, X. Zhang, J.-J. Zou, Solid-acid-mediated electronic structure regulation of electrocatalysts and scaling relation breaking of oxygen evolution reaction, Appl. Catal. B 277 (2020), 119237.

[24] Y. Shi, W. Du, W. Zhou, C. Wang, S. Lu, S. Lu, B. Zhang, Unveiling the promotion of surface-adsorbed chalcogenate on the electrocatalytic oxygen evolution reaction, Angew. Chem. Int. Ed. 59 (2020) 22470–22474.

[25] S. Li, Z. Li, R. Ma, C. Gao, L. Liu, L. Hu, J. Zhu, T. Sun, Y. Tang, D. Liu, J. Wang, A glass-ceramic with accelerated surface reconstruction toward the efficient oxygen evolution reaction, Angew. Chem. Int. Ed. 60 (2021) 3773–3780.

[26] Y. Zuo, Y. Liu, J. Li, R. Du, X. Han, T. Zhang, J. Arbiol, N.J. Divins, J. Llorca, N. Guijarro, In situ electrochemical oxidation of Cu₂S into CuO nanowires as a durable and efficient electrocatalyst for oxygen evolution reaction, Chem. Mater. 31 (2019) 7732–7743.

[27] G. Chen, Y. Zhu, H.M. Chen, Z. Hu, S.F. Hung, N. Ma, J. Dai, H.J. Lin, C.T. Chen, W. Zhou, Z. Shao, An amorphous nickel-iron-based electrocatalyst with unusual local structures for ultrafast oxygen evolution reaction, Adv. Mater. 31 (2019), 1900883.

[28] J. Liu, Y. Ji, J. Nai, X. Niu, Y. Luo, L. Guo, S. Yang, Ultrathin amorphous cobalt–vanadium hydr(oxy)oxide catalysts for the oxygen evolution reaction, Energy Environ. Sci. 11 (2018) 1736–1741.

[29] S. Anantharaj, S. Noda, Amorphous catalysts and electrochemical water splitting: an untold story of harmony, Small 16 (2020), 1905779.

[30] J. Kwon, H. Han, S. Jo, S. Choi, K.Y. Chung, G. Ali, K. Park, U. Paik, T. Song, Amorphous nickel–iron borophosphate for a robust and efficient oxygen evolution reaction, Adv. Energy Mater. 11 (2021), 2100624.

[31] X. Li, L. Xiao, L. Zhou, Q. Xu, J. Weng, J. Xu, B. Liu, Adaptive bifunctional electrocatalyst of amorphous CoFe oxide@ 2D black phosphorus for overall water splitting, Angew. Chem. Int. Ed. 132 (2020) 21292–21299.

[32] X. Wang, C. Xing, Z. Liang, P. Guardia, X. Han, Y. Zuo, J. Llorca, J. Arbiol, J. Li, A. Cabot, Activating the lattice oxygen oxidation mechanism in amorphous molybdenum cobalt oxide nanosheets for water oxidation, J. Mater. Chem. A 10 (2022) 3659–3666.

[33] Z.J. Chen, T. Zhang, X.Y. Gao, Y.J. Huang, X.H. Qin, Y.F. Wang, K. Zhao, X. Peng, C. Zhang, L. Liu, M.H. Zeng, H.B. Yu, Engineering microdomains of oxides in high-entropy alloy electrodes toward efficient oxygen evolution, Adv. Mater. 33 (2021), 2101845.

[34] J. Bai, J. Mei, T. Liao, Q. Sun, Z.G. Chen, Z. Sun, Molybdenum-promoted surface reconstruction in polymorphic cobalt for initiating rapid oxygen evolution, Adv. Energy Mater. 12 (2021), 2103247.

[35] J. Zhang, T. Quast, W. He, S. Dieckhöfer, J.R. Junqueira, D. Öhl, P. Wilde, D. Jambrec, Y.T. Chen, W. Schuhmann, In-situ carbon corrosion and Cu leaching as a strategy for boosting oxygen evolution reaction in multi-metal electrocatalysts, Adv. Mater. 34 (2022), 2109108.

[36] S. Wahl, S.M. El-Refaei, A.G. Buzanich, P. Amsalem, K.S. Lee, N. Koch, M. L. Doublet, N. Pinna, Zn₀.₃₅Co₀.₆₅O⁻A stable and highly active oxygen evolution catalyst formed by zinc leaching and tetrahedral coordinated cobalt in wurtzite structure, Adv. Energy Mater. 9 (2019), 1900328.

[37] X.F. Lu, Y. Fang, D. Luan, X.W.D. Lou, Metal–organic frameworks derived functional materials for electrochemical energy storage and conversion: a mini review, Nano Lett. 21 (2021) 1555–1565.

[38] M. Yang, C.H. Zhang, N.W. Li, D.Y. Luan, L. Yu, X.W. Lou, Design and synthesis of hollow nanostructures for electrochemical water splitting, Adv. Sci. 9 (2022), 2105135.

[39] W. Wang, H. Yan, U. Anand, U. Mirsaidov, Visualizing the conversion of metal–organic framework nanoparticles into hollow layered double hydroxide nanocages, J. Am. Chem. Soc. 143 (2021) 1854–1862.

[40] W. Cheng, Z.P. Wu, D. Luan, S.Q. Zang, X.W. Lou, Synergetic cobalt-copper-based bimetal–organic framework nanoboxes toward efficient electrochemical oxygen evolution, Angew. Chem. Int. Ed. 60 (2021) 26397–26402.

[41] Y. Huang, S.L. Zhang, X.F. Lu, Z.P. Wu, D. Luan, X.W.D. Lou, Trimetallic spinel NiCo₂₋ₓFeₓO₄ nanoboxes for highly efficient electrocatalytic oxygen, Evol., Angew. Chem. Int. Ed. 60 (2021) 11841–11846.

[42] C. Qiao, Z. Usman, T. Cao, S. Rafai, Z. Wang, Y. Zhu, C. Cao, J. Zhang, High-valence Ni and Fe sites on sulfated NiFe-LDH nanosheets to enhance O-O coupling for water oxidation, Chem. Eng. J. 426 (2021), 130873.

[43] N.V. Chukanov, A.D. Chervonnyi, Infrared Spectroscopy of Minerals and Related Compounds, Springer, 2016.

[44] G. Wu, X. Zheng, P. Cui, H. Jiang, X. Wang, Y. Qu, W. Chen, Y. Lin, H. Li, X. Han, A general synthesis approach for amorphous noble metal nanosheets, Nat. Commun. 10 (2019) 1–8.

[45] C.C. McCrory, S. Jung, J.C. Peters, T.F. Jaramillo, Benchmarking heterogeneous electrocatalysts for the oxygen evolution reaction, J. Am. Chem. Soc. 135 (2013) 16977–16987.

[46] S.L. Zhang, B.Y. Guan, X.F. Lu, S. Xi, Y. Du, X.W.D. Lou, Metal atom-doped Co₃O₄ hierarchical nanoplates for electrocatalytic oxygen evolution, Adv. Mater. 32 (2020), 2002235.

[47] Z.-F. Huang, J. Song, Y. Du, S. Xi, S. Dou, J.M.V. Nsanzimana, C. Wang, Z.J. Xu, X. Wang, Chemical and structural origin of lattice oxygen oxidation in Co–Zn oxyhydroxide oxygen evolution electrocatalysts, Nat. Energy 4 (2019) 329–338.

[48] M. Fang, D. Han, W.B. Xu, Y. Shen, Y. Lu, P. Cao, S. Han, W. Xu, D. Zhu, W. Liu, Surface-guided formation of amorphous mixed-metal oxyhydroxides on ultrathin MnO₂ nanosheet arrays for efficient electrocatalytic oxygen evolution, Adv. Energy Mater. 10 (2020), 2001059.

[49] S.Y. Lim, S. Park, S.W. Im, H. Ha, H. Seo, K.T. Nam, Chemically deposited amorphous Zn-doped NiFeOₓHᵧ for enhanced water oxidation, ACS Catal. 10 (2019) 235–244.

[50] Y. Duan, S. Sun, S. Sun, S. Xi, X. Chi, Q. Zhang, X. Ren, J. Wang, S.J.H. Ong, Y. Du, L. Gu, A. Grimaud, Z.J. Xu, Mastering surface reconstruction of metastable spinel oxides for better water oxidation, Adv. Mater. 31 (2019), 1807898.

[51] T. Ling, T. Zhang, B. Ge, L. Han, L. Zheng, F. Lin, Z. Xu, W.B. Hu, X.W. Du, K. Davey, S.Z. Qiao, Well-dispersed nickel- and zinc-tailored electronic structure of a transition metal oxide for highly active alkaline hydrogen evolution reaction, Adv. Mater. 31 (2019), e1807771.

[52] Y. Sun, X. Ren, S. Sun, Z. Liu, S. Xi, Z.J. Xu, Engineering high-spin state cobalt cations in spinel zinc cobalt oxide for spin channel propagation and active site enhancement in water oxidation, Angew. Chem. Int. Ed. 60 (2021) 14536–14544.

[53] A. Bergmann, T.E. Jones, E. Martinez Moreno, D. Teschner, P. Chernev, M. Gliech, T. Reier, H. Dau, P. Strasser, Unified structural motifs of the catalytically active state of Co (oxyhydr) oxides during the electrochemical oxygen evolution reaction, Nat. Catal. 1 (2018) 711–719.

[54] J. He, X. Zhou, P. Xu, J. Sun, Promoting electrocatalytic water oxidation through tungsten-modulated oxygen vacancies on hierarchical FeNi-layered double hydroxide, Nano Energy 80 (2021), 105540.

[55] L. Zhang, C. Lu, F. Ye, Z. Wu, Y. Wang, L. Jiang, L. Zhang, C. Cheng, Z. Sun, L. Hu, Vacancies boosting strategy enabling enhanced oxygen evolution activity in a library of novel amorphous selenite electrocatalysts, Appl. Catal. B 284 (2021), 119758.

[56] D. Guan, G. Ryu, Z. Hu, J. Zhou, C.L. Dong, Y.C. Huang, K. Zhang, Y. Zhong, A. C. Komarek, M. Zhu, X. Wu, C.W. Pao, C.K. Chang, H.J. Lin, C.T. Chen, W. Zhou, Z. Shao, Utilizing ion leaching effects for achieving high oxygen-evolving performance on hybrid nanocomposite with self-optimized behaviors, Nat. Commun. 11 (2020) 3376.

[57] R.I. Sayler, B.M. Hunter, W. Fu, H.B. Gray, R.D. Britt, EPR spectroscopy of iron-and nickel-doped [ZnAl]-layered double hydroxides: modeling active sites in heterogeneous water oxidation catalysts, J. Am. Chem. Soc. 142 (2019) 1838–1845.

[58] J. Wang, J. Liu, B. Zhang, F. Cheng, Y. Ruan, X. Ji, K. Xu, C. Chen, L. Miao, J. Jiang, Stabilizing the oxygen vacancies and promoting water-oxidation kinetics in cobalt oxides by lower valence-state doping, Nano Energy 53 (2018) 144–151.

[59] W. Xu, W. Gao, L. Meng, W. Tian, L. Li, Incorporation of sulfate anions and sulfur vacancies in ZnIn₂S₄ photoanode for enhanced photoelectrochemical water splitting, Adv. Energy Mater. 11 (2021), 2101181.